THE ASTROPHYSICAL JOURNAL SUPPLEMENT SERIES, 92:145–161, 1994 May

OUTFLOWS FROM YOUNG STELLAR OBJECTS IN BOK GLOBULES: MAPS

JOÃO LIN YUN
Departamento de Física, Universidade de Lisboa, Campo Grande, Ed. C1, Piso 4, 1700 Lisboa, Portugal
AND
DAN P. CLEMENS
Astronomy Department, Boston University, 725 Commonwealth Avenue, Boston, MA 02215
Received 10 May 1993; Accepted: 1993 September 29

ABSTRACT

We have obtained ^{12}CO $J = 1$–0 spectral line maps of high-velocity gas outflows from a sample of 14 small Bok globules containing low-mass young stellar objects (YSOs). The observations were performed using the new 15 beam receiver (QUARRY) of the Five College Radio Astronomy Observatory.

Morphologically, the outflows in our sample exhibit small angular extents, and relatively wide angular lobes with the majority exhibiting low apparent degrees of collimation.

The presence of an outflow was found to be correlated with the value of the *IRAS*-based spectral index (between 12 and 25 μm) of the YSOs. Outflows were more frequently detected in those globules with the reddest *IRAS* point sources. These spectral indices are consistent with emission from objects in fairly early stages of the star formation process which are still deeply embedded in gas and dust.

Energetically, the outflows in our sample may be among the weakest and least massive found to date. Nevertheless, both the outflow kinematics and energetics indicate that they may play an important role in cloud support and evolution.

Subject headings: ISM: jets and outflows — ISM: molecules — radio lines: ISM — stars: formation —stars: pre–main-sequence

1. INTRODUCTION

Star formation has been widely studied in giant molecular clouds or complexes of dark clouds where the very conspicuous massive star formation is known to take place. Investigations of star formation in small clouds has been comparatively less studied. Part of the current knowledge of the details of star formation has emerged from the discovery and subsequent study of the phenomenon of high-velocity mass ejection from young stellar objects (YSOs) in molecular clouds, which often consists of bipolar molecular winds or outflows. However, until recently, few outflows had been found associated with low-mass YSOs in small molecular clouds. The discovery and investigation of these flows and their driving sources could help answer some of the questions related to star formation, such as:

Do all young stellar objects undergo an episode of bipolar mass ejection (outflow)? What is the role of an outflow in the evolution of a young star? Are the mechanical forces of the outflows large enough to have pronounced effects on subsequent star formation and stability of the molecular clouds, as proposed by Silk & Norman (1980) and Schwartz, Gee, & Huang (1988)? Can outflows be the agent of dispersal of the circumstellar material, responsible for halting accretion onto the forming star, limiting the amount of mass that can be accreted, or aiding the transition from an embedded, optically invisible object to an optically visible pre–main-sequence star, as suggested by Bally & Lada (1983)?

In order to address some of these questions, we have investigated the nature of YSOs in a set of small molecular clouds (mostly Bok globules). In our recent *IRAS* survey of point sources associated with the Bok globules cataloged by Clemens & Barvainis (1988, hereafter CB), we found that a surprisingly large number of Bok globules show evidence for associated point sources (Yun & Clemens 1990, hereafter YC90). From a comparison of the 12 and 25 μm fluxes of these objects, we found a distribution of 12/25 μm spectral indices consistent with the presence of circumstellar dust, implying that the population is dominated by young stellar objects.

Since Lada's (1985) catalog of high-velocity outflows, increasing numbers of outflows associated with YSOs in small molecular clouds have been found. These surveys looked for CO outflows near dense cores (Myers et al. 1988) or near pre–main-sequence stars (Levreault 1988). Parker, Padman, & Scott (1991) surveyed a set of 12 Lynds (1962) dark clouds showing evidence of embedded *IRAS* point sources, identifying seven new outflows.

In a previous paper (Yun & Clemens 1992, hereafter YC92) we reported the discovery of CO outflows associated with our recently discovered YSOs in Bok globules. Forty-one Bok globules were surveyed for outflows in the $J = 1$–0 line of ^{12}CO using QUARRY (*Qua*bbin *Arr*ay *R*eceiver), the new 15 beam focal plane array receiver (Erickson et al. 1992) of the Five College Radio Astronomy Observatory (FCRAO). Thirty-six of these globules contained a total of 39 *IRAS* point sources. Of these 39 sources, 14 were found to show signs of CO outflows. Of the remaining five control sources (no *IRAS* point sources), none showed outflows. The presence of outflows seemed to occur in the younger, more embedded objects (Class I objects in the classification scheme proposed by Lada 1987), as estimated by their 12/25 μm spectral indices.

In this paper we present maps of the 14 outflows (12 newly discovered) obtained with Nyquist spatial sampling (25″ resolution), as well as improved estimates of derived outflow properties.

In the next few sections we present the observations and discuss and summarize the results.

2. OBSERVATIONS AND RESULTS

In 1991 October 22 to 27, we used QUARRY to observe the 14 outflows at FCRAO, mapping the clouds at half-beam spacing (Nyquist sampling) with a total integration time at CO of 30 minutes per position. At a frequency of 115 GHz (^{12}CO, $J = 1$–0), the antenna had beamwidths of 48″ (FWHM). The spectrometer was a 15 × 32 channel 250 kHz filter bank and provided a velocity resolution of 0.65 km s^{-1} channel^{-1}. The rms noise per channel in the final spectra was 0.15 K (T_A^*) or less. In addition, we observed three globules (CB 3, CB 205, and CB 216) in the $J = 1$–0 line of ^{13}CO with full-beam spacing. Data for cloud maps were collected in position-switched mode using reference positions previously verified to be emission free. Pointing was checked by observing the planets and calibration was done by continuum scanning across Jupiter. The main beam efficiency was measured to be ~45%.

For each globule YSO listed in Table 1, we collected 120 spectra using eight sky placements of QUARRY. The nomenclature used in Table 1 indicates the Bok globule CB number (CB) followed by the *Y*oung stellar object *C*andidate number (e.g., CB 205/YC 1). The final maps covered ~8′ in R. A. and 6′ in Dec., with Nyquist sampling. Figure 1 shows the approximate positions of the beam placements on the sky (marked by crosses) and the beam size (circle). After elimination of a few bad channels, linear baselines were fitted and removed from the spectra.

As stated in YC92, we have adopted the following criteria to judge whether an outflow could be inferred from the velocity structure seen in each cloud: First, we required that at least one of the CO spectra for a source had a clearly non-Gaussian shape, displaying wings extending away from the line core. Second, for the spectra which were non-Gaussian, we determined the signal-to-noise ratio in the wings and considered only the cases with a signal exceeding 3 times the corresponding noise level. Three cases, CB 81, CB 230, and CB 247, with signal levels of 2 σ, were additionally accepted due to the clearly extended wings displayed by some of their spectra. Third, the velocity extent had to be larger than 3 km s^{-1} beyond that of the quiescent gas.

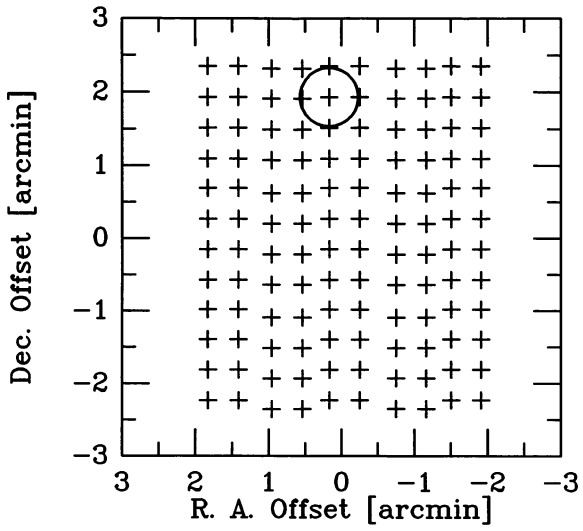

FIG. 1.—The placements of the FCRAO telescope beams on the sky relative to the center positions given in Table 1. The circle shows the FWHM beam size. The not-quite-uniform sampling grid is due to a minor misalignment of the two QUARRY feed horn subarrays.

TABLE 1

YSO SAMPLE POSITIONS

Cloud/YSO (1)	R. A. (1950) (2)	Decl. (1950) (3)	Position Ref. (4)
CB 3/YC 1	00^{h}25^{m}59^s	56°25′32″	PSC 00259+5625
CB 34/YC 1	05^{h}44^{m}03^s	20°59′07″	PSC 05440+2059
CB 39/YC 1	05^{h}59^{m}06^s	16°30′58″	PSC 05591+1630
CB 54/YC 1	07^{h}02^{m}06^s	−16°18′47″	PSC 07020−1618
CB 81/YC 1	17^{h}19^{m}19^s	−27°05′20″	YC 92
CB 188/YC 1	19^{h}17^{m}57^s	11°30′18″	YC 92
CB 205/YC 1	19^{h}43^{m}22^s	27°44′01″	YC 92
CB 214/YC 1	20^{h}01^{m}54^s	26°29′42″	YC 92
CB 216/YC 1	20^{h}03^{m}45^s	23°18′25″	YC 92
CB 217/YC 1	20^{h}05^{m}55^s	36°58′14″	YC 92
CB 230/YC 1	21^{h}16^{m}55^s	68°04′52″	PSC 21169+6804
CB 232/YC 1	21^{h}35^{m}14^s	43°07′05″	PSC 21352+4307
CB 244/YC 1	23^{h}23^{m}49^s	74°01′08″	PSC 23238+7401
CB 247/YC 1	23^{h}55^{m}04^s	64°30′10″	PSC 23550+6430

Figure 2 shows an example of the resulting CO spectra toward one globule-YSO. The spectra in this figure were obtained toward the YSO in CB 205 (L810; Yun et al. 1993) and are presented in their relative spatial positions. Notice the wide line wings (mostly blue) near the center of the map and the narrow lines at the periphery.

Figures 3–16 show details of some of the spectra for each outflow source, chosen to exhibit representative wing emission (usually obtained toward the center of the map) together with a spectrum obtained toward more quiescent cloud material (usually from the edge of the map). For each source, line shape comparisons were performed between the spectra exhibiting wing emission and a mean spectrum formed by averaging the nonoutflow spectra obtained toward the more quiescent cloud material.

In Figures 17–29, contour maps of the integrated line wing emission toward each globule-YSO are presented. In these figures, edge effects are due to the algorithm used to construct the contour lines and have no significance.

A brief discussion of the spectra and maps for each globule/YSO follows.

2.1. *CB 3/YC 1*

Figure 17*a* shows the contour map of the ^{13}CO integrated emission from the globule CB 3 (= LBN 594), revealing the location of the core of the globule. The triangle marks the position of the *IRAS* PSC source (*IRAS* 00259+5625) corresponding to the YSO CB 3/YC 1. The contour map of the

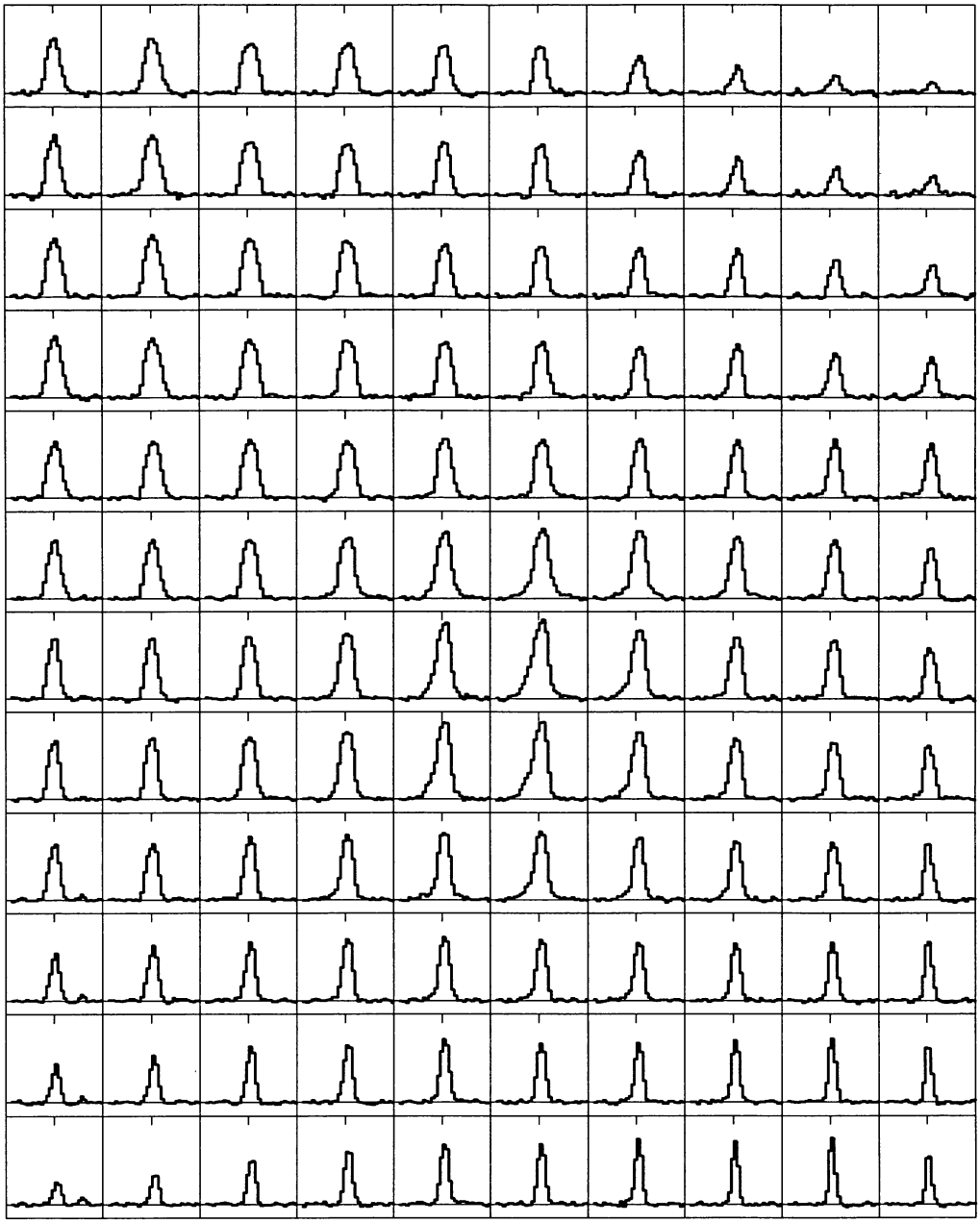

FIG. 2.—Map of ^{12}CO emission line profiles for CB 205. The spectra are presented in their relative angular positions. The horizontal velocity axis and the vertical antenna temperature axis are the same as in Figure 9.

blueshifted (solid lines) and the redshifted (dashed lines) integrated CO wing emission for the same YSO is displayed in Figure 17*b*. In this map, the blue and the red lobes overlap significantly and exhibit peaks which are close to each other. The outflow exhibits a poor degree of collimation at this angular resolution. Individual spectra are rather symmetric, displaying both blue and red wings at the same position, extending $\sim$7 km s^{-1} away from the line center (Fig. 3).

The center of the flow coincides with the core of the globule as traced by ^{13}CO emission. The outflow orientation is roughly parallel to the elongation direction for the ^{13}CO core (position angle $\sim$0°). The *IRAS* point source is less than 0.5 east of the center of the flow and is very likely the outflow source. It has a 12/25 spectral index

$$\left[\alpha = \frac{d \log (\nu S_\nu)}{d \log \nu}\right]$$

of 0.90 (i.e., fairly blue for a YSO; YC 90) and inspection of the red Palomar plates (POSS) reveals the presence of an optically visible star at this position. There is also a water maser detected toward the PSC position (Scappini et al. 1991).

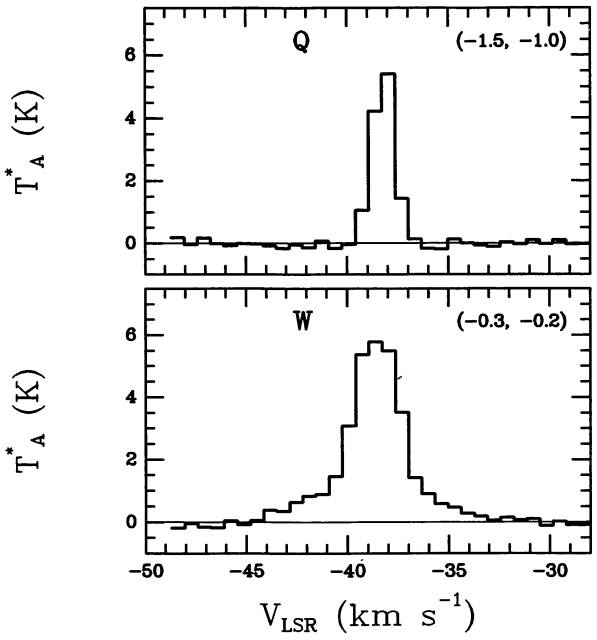

FIG. 3.—Representative spectra for CB 3/YC 1. The lower panel shows the presence of wing emission ("W") and non-Gaussian lines. A spectrum obtained toward more quiescent cloud material ("Q") is also included for comparison (*upper panel*). The coordinates at the upper right corner identify the angular offset position ($\Delta\alpha, \Delta\delta$) in arcminutes of the spectrum relative to the coordinates in Table 1.

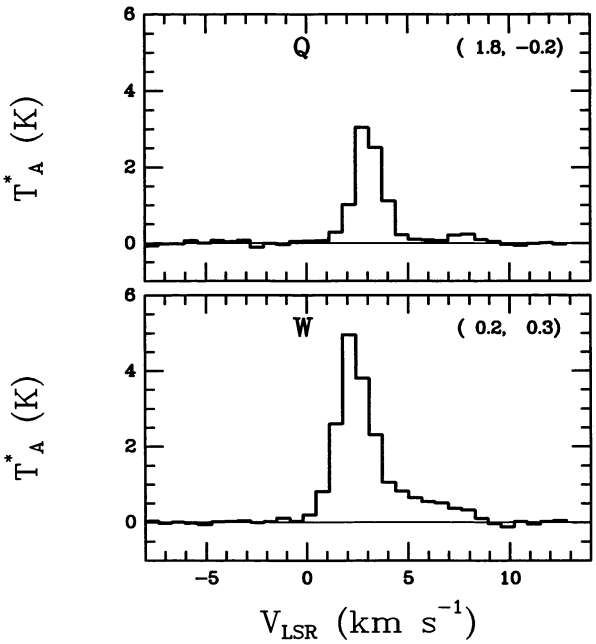

FIG. 5.—Representative spectra for CB 39/YC 1. The lower panel shows the presence of wing emission ("W") and non-Gaussian lines. A spectrum obtained toward more quiescent cloud material ("Q") is also included for comparison (*upper panel*). The coordinates at the upper right corner identify the angular offset position of the spectrum relative to the coordinates in Table 1.

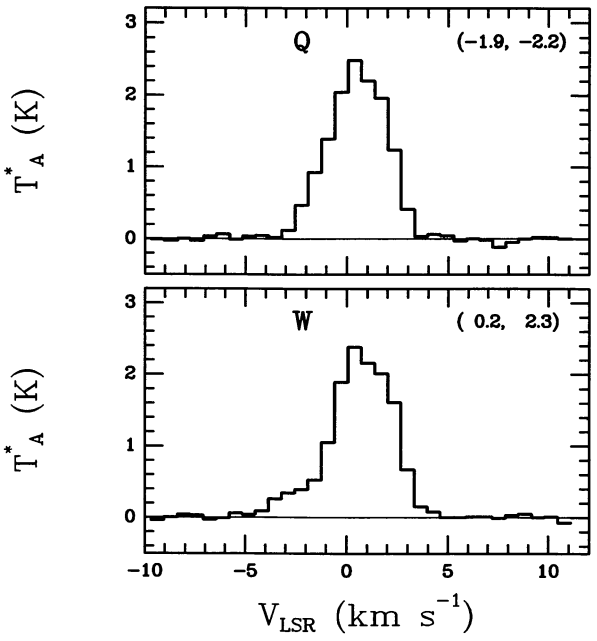

FIG. 4.—Representative spectra for CB 34/YC 1. The lower panel shows the presence of wing emission ("W") and non-Gaussian lines. A spectrum obtained toward more quiescent cloud material ("Q") is also included for comparison (*upper panel*). The coordinates at the upper right corner identify the angular offset position of the spectrum relative to the coordinates in Table 1.

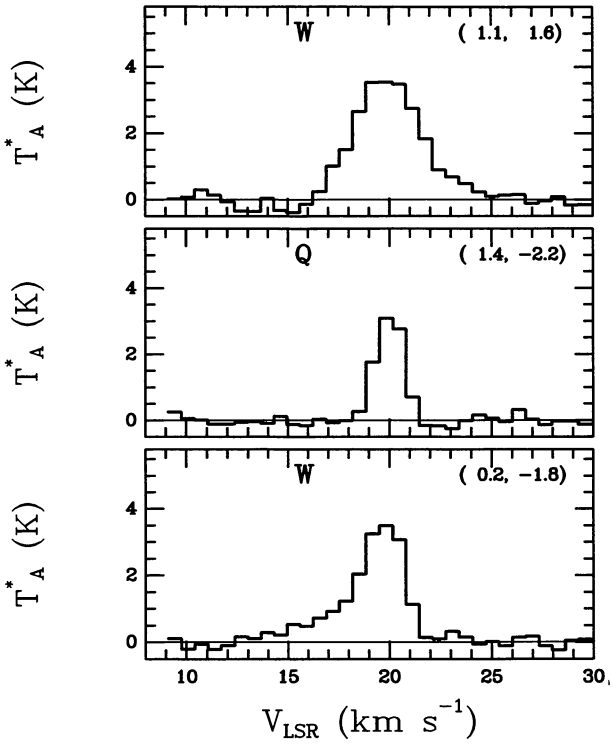

FIG. 6.—Representative spectra for CB 54/YC 1. The upper and lower panels show the presence of wing emission ("W"), red and blue, respectively, and non-Gaussian lines. A spectrum obtained toward more quiescent cloud material ("Q") is also included for comparison (*middle panel*). The coordinates at the upper right corner identify the angular offset position of the spectrum relative to the coordinates in Table 1.

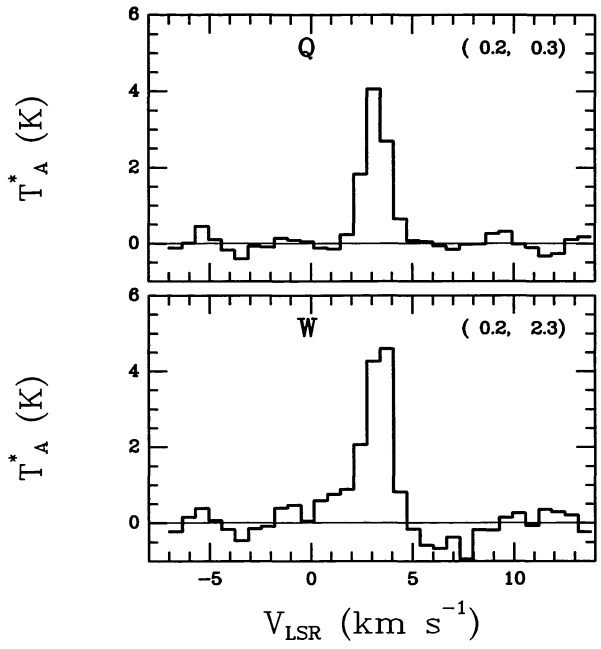

FIG. 7.—Representative spectra for CB 81/YC 1. The *lower panel* shows the presence of wing emission ("W") and non-Gaussian lines. A spectrum obtained toward more quiescent cloud material ("Q") is also included for comparison (*upper panel*). The coordinates at the upper right corner identify the angular offset position of the spectrum relative to the coordinates in Table 1.

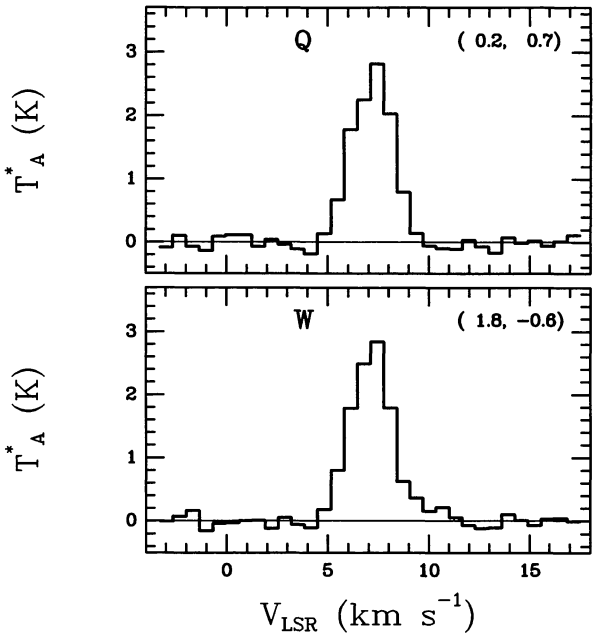

FIG. 9.—Representative spectra for CB 205/YC 1. The lower panel shows the presence of wing emission ("W") and non-Gaussian lines. A spectrum obtained toward more quiescent cloud material ("Q") is also included for comparison (*upper panel*). The coordinates at the upper right corner identify the angular offset position of the spectrum relative to the coordinates in Table 1.

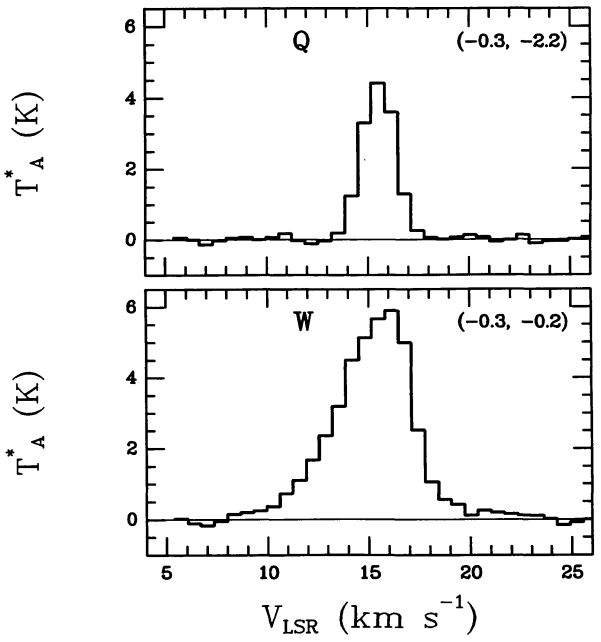

FIG. 8.—Representative spectra for CB 188/YC 1. The lower panel shows the presence of wing emission ("W") and non-Gaussian lines. A spectrum obtained toward more quiescent cloud material ("Q") is also included for comparison (*upper panel*). The coordinates at the upper right corner identify the angular offset position of the spectrum relative to the coordinates in Table 1.

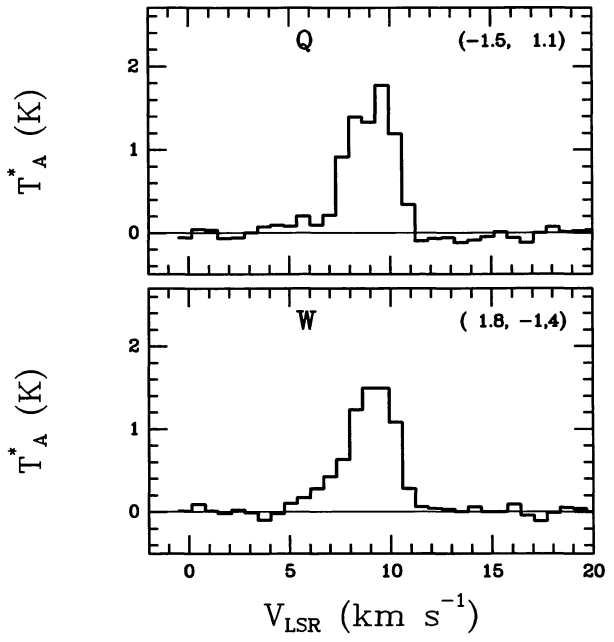

FIG. 10.—Representative spectra for CB 214/YC 1. The lower panel shows the presence of wing emission ("W") and non-Gaussian lines. A spectrum obtained toward more quiescent cloud material ("Q") is also included for comparison (*upper panel*). The coordinates at the upper right corner identify the angular offset position of the spectrum relative to the coordinates in Table 1.

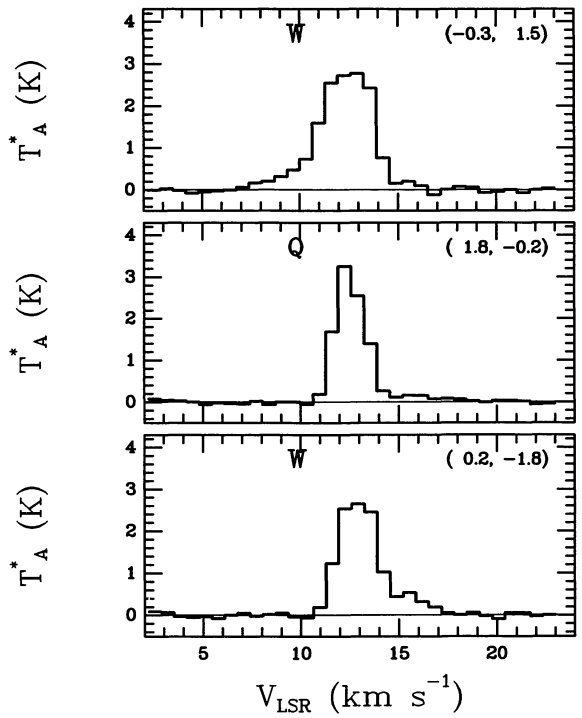

FIG. 11.—Representative spectra for CB 216/YC 1. The upper and lower panels show the presence of wing emission ("W"), blue and red, respectively, and non-Gaussian lines. A spectrum obtained toward more quiescent cloud material ("Q") is also included for comparison (*middle panel*). The coordinates at the upper right corner identify the angular offset position of the spectrum relative to the coordinates in Table 1.

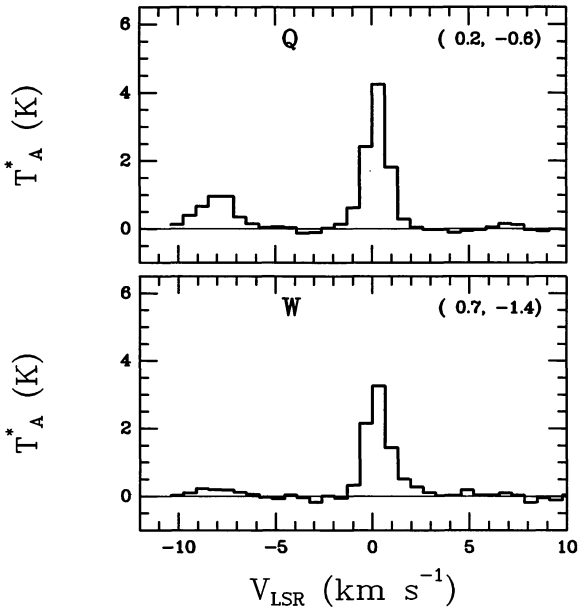

FIG. 12.—Representative spectra for CB 217/YC 1. The lower panel shows the presence of wing emission ("W") and non-Gaussian lines. A spectrum obtained toward more quiescent cloud material ("Q") is also included for comparison (*upper panel*). The coordinates at the upper right corner identify the angular offset position of the spectrum relative to the coordinates in Table 1. The component at $v = -8.5$ km s^{-1} is likely due to unrelated emission along the same line of sight.

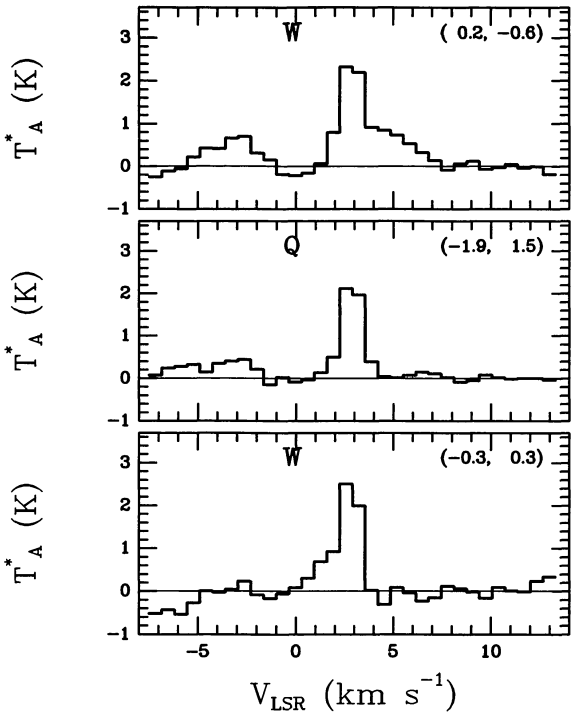

FIG. 13.—Representative spectra for CB 230/YC 1. The upper and lower panels show the presence of wing emission ("W"), red and blue, respectively, and non-Gaussian lines. A spectrum obtained toward more quiescent cloud material ("Q") is also included for comparison (*middle panel*). The coordinates at the upper right corner identify the angular offset position of the spectrum relative to the coordinates in Table 1. The component at $v = -3.0$ km s^{-1} is likely due to unrelated emission along the same line of sight.

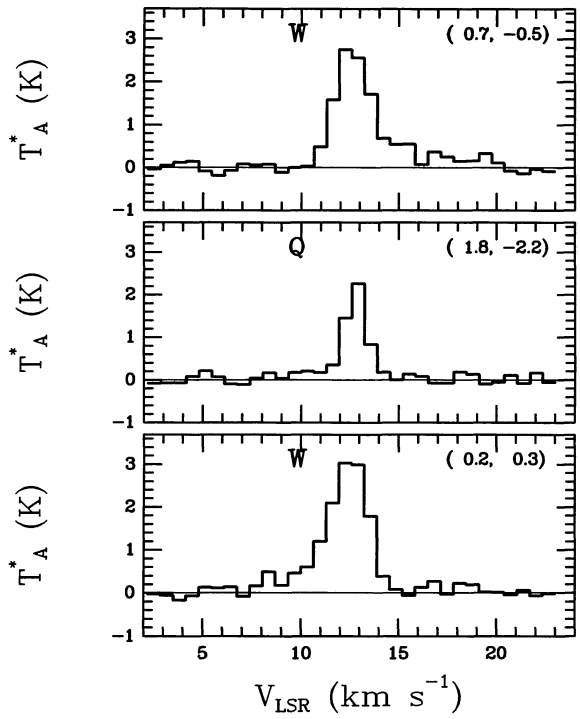

FIG. 14.—Representative spectra for CB 232/YC 1. The upper and lower panels show the presence of wing emission ("W"), red and blue respectively, and non-Gaussian lines. A spectrum obtained toward more quiescent cloud material ("Q") is also included for comparison (*middle panel*). The coordinates at the upper right corner identify the angular offset position of the spectrum relative to the coordinates in Table 1.

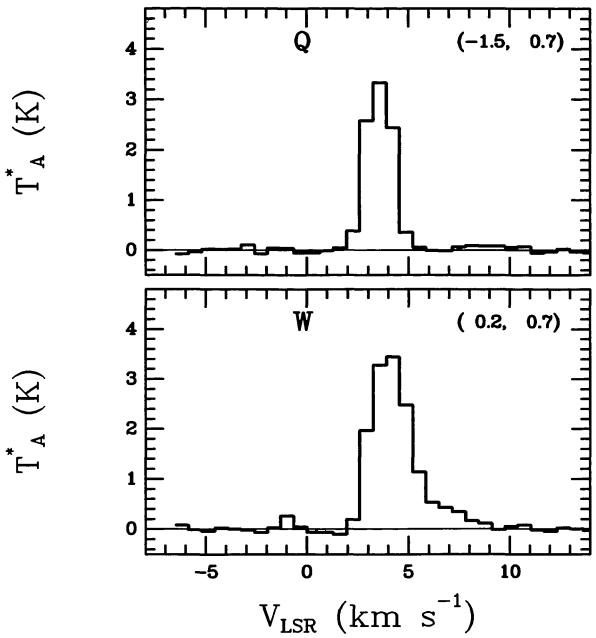

FIG. 15.—Representative spectra for CB 244/YC 1. The lower panel shows the presence of wing emission ("W") and non-Gaussian lines. A spectrum obtained toward more quiescent cloud material ("Q") is also included for comparison (*upper panel*). The coordinates at the upper right corner identify the angular offset position of the spectrum relative to the coordinates in Table 1.

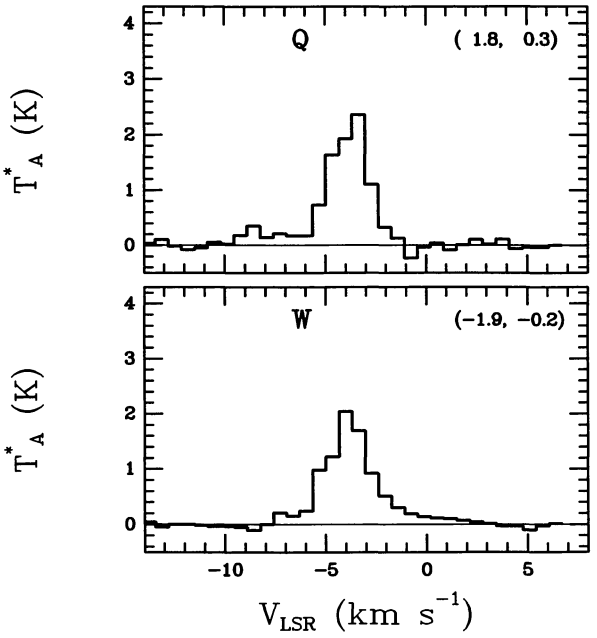

FIG. 16.—Representative spectra for CB 247/YC 1. The lower panel shows the presence of wing emission ("W") and non-Gaussian lines. A spectrum obtained toward more quiescent cloud material ("Q") is also included for comparison (*upper panel*). The coordinates at the upper right corner identify the angular offset position of the spectrum relative to the coordinates in Table 1.

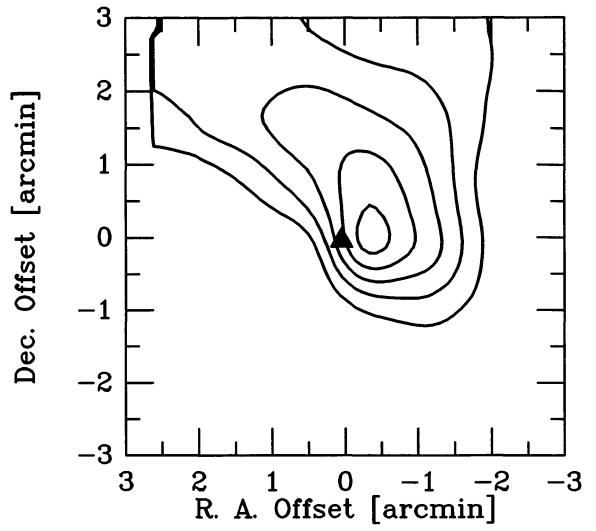

FIG. 17*a*

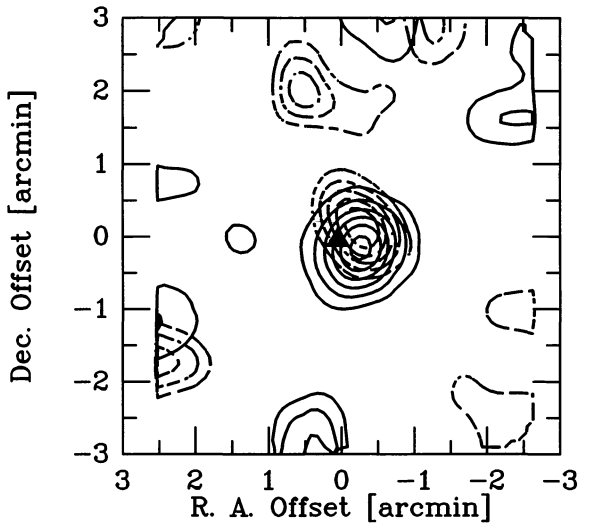

FIG. 17*b*

FIG. 17.—(*a*) Contour plot of the ^{13}CO integrated line emission $\int T_A^* dV$ for CB 3/YC 1. Contours begin at 2 K km s^{-1} and are stepped by 1 K km s^{-1}. The position of the *IRAS* PSC source is marked by a filled triangle. (*b*) Contour plot of the blue (*solid lines*) and the red (*dashed lines*) integrated line wing emission associated with CB 3/YC 1. The velocity intervals of integration were (−45, −41) and (−36, −31) km s^{-1} for the blue and the red wings, respectively. Blue contours begin at 0.3 K km s^{-1} and are stepped by 0.2 K km s^{-1}. Red contours begin at 0.4 K km s^{-1} and are stepped by 0.15 K km s^{-1}. The position of the *IRAS* PSC source is marked by a filled triangle.

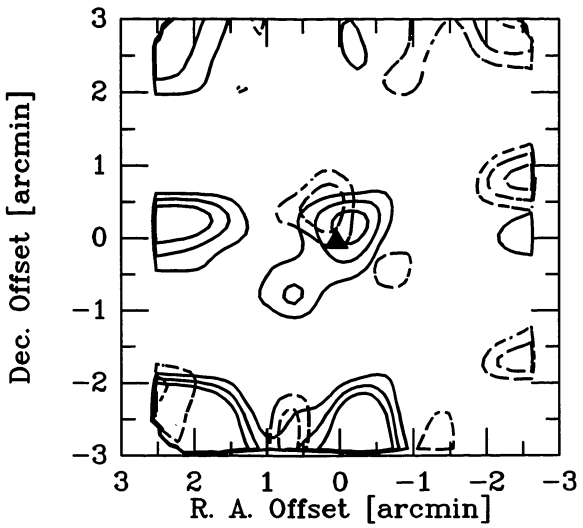

FIG. 18.—Contour plot of the blue (*solid lines*) and the red (*dashed lines*) integrated line wing emission associated with CB 34/YC 1. The velocity intervals of integration were (−7,−2) and (3,8) km s^{-1} for the blue and the red wings, respectively. Blue contours begin at 0.5 K km s^{-1} and are stepped by 0.1 K km s^{-1}. Red contours begin at 0.8 K km s^{-1} and are stepped by 0.2 K km s^{-1}. The position of the *IRAS* PSC source is marked by a filled triangle.

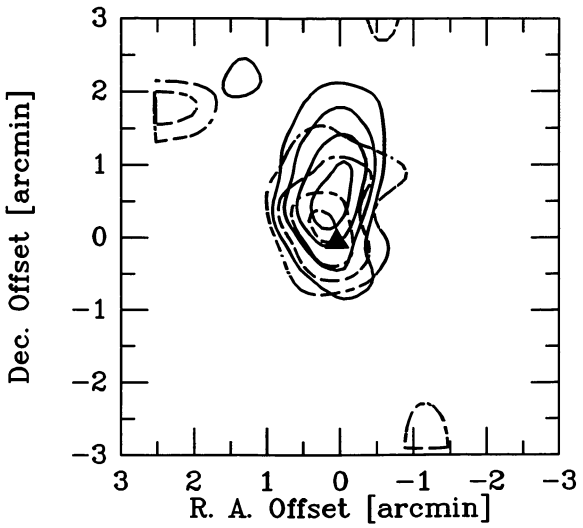

FIG. 19.—Contour plot of the blue (*solid lines*) and the red (*dashed lines*) integrated line wing emission associated with CB 39/YC 1. The velocity intervals of integration were (−2.5, 1.5) and (5,9) km s^{-1} for the blue and the red wings, respectively. Contours for both wings begin at 0.8 K km s^{-1} and are stepped by 0.2 K km s^{-1}. The position of the *IRAS* PSC source is marked by a filled triangle.

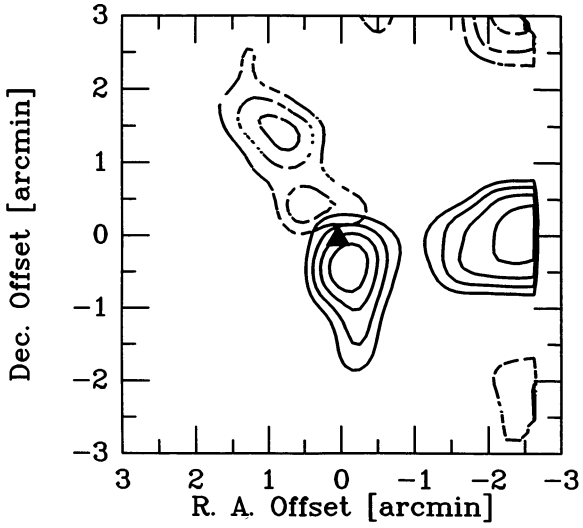

FIG. 20.—Contour plot of the blue (*solid lines*) and the red (*dashed lines*) integrated line wing emission associated with CB 54/YC 1. The velocity intervals of integration were (13,17) and (23,27) km s^{-1} for the blue and the red wings, respectively. Blue contours begin at 1.7 K km s^{-1} and are stepped by 0.3 K km s^{-1}. Red contours begin at 0.45 K km s^{-1} and are stepped by 0.15 K km s^{-1}. The position of the *IRAS* PSC source is marked by a *filled triangle.*

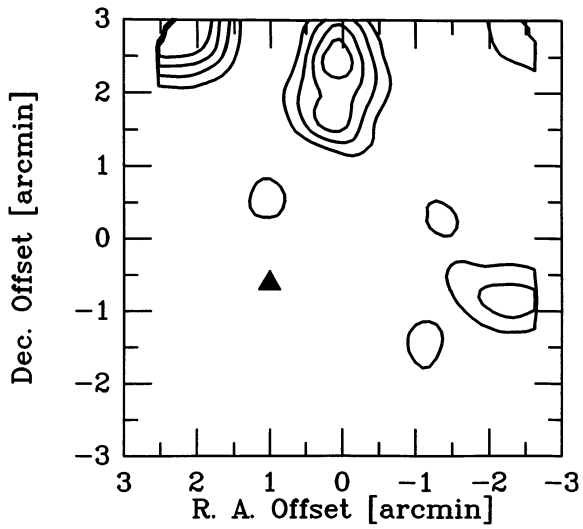

FIG. 21.—Contour plot of the blue integrated line wing emission associated with CB 81/YC 1. The interval of integration was (−1,2) km s^{-1}. Contours begin at 0.5 K km s^{-1} and are stepped by 0.25 K km s^{-1}. The position of the *IRAS* PSC source is marked by a filled triangle.

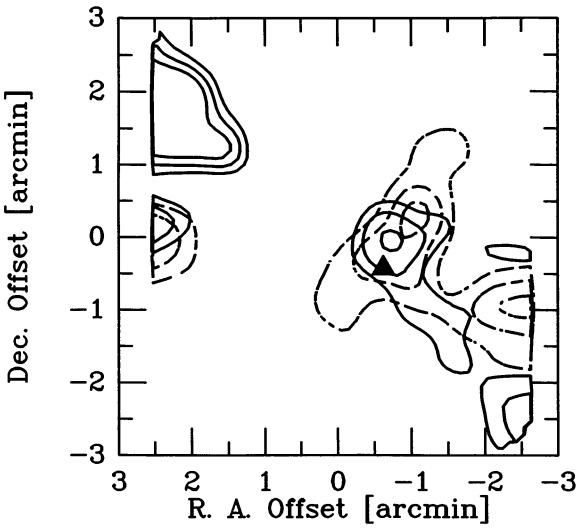

FIG. 22.—Contour plot of the blue (*solid lines*) and the red (*dashed lines*) integrated line wing emission associated with CB 188/YC 1. The velocity intervals of integration were (1.5,5.5) and (9,14) km s^{-1} for the blue and the red wings, respectively. Blue contours begin at 0.7 K km s^{-1} and are stepped by 0.1 K km s^{-1}. Red contours begin at 0.6 K km s^{-1} and are stepped by 0.2 K km s^{-1}. The position of the *IRAS* PSC source is marked by a filled triangle.

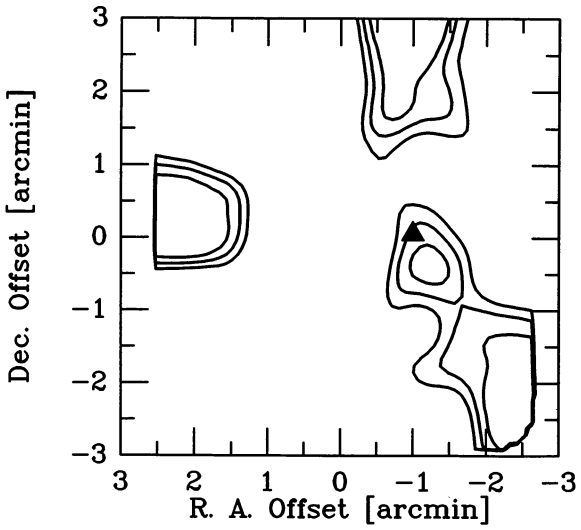

FIG. 24.—Contour plot of the blue integrated line wing emission associated with CB 214/YC 1. The interval of integration was (2,7) km s^{-1}. Contours begin at 1.0 K km s^{-1} and are stepped by 0.1 K km s^{-1}. The position of the *IRAS* PSC source is marked by a filled triangle.

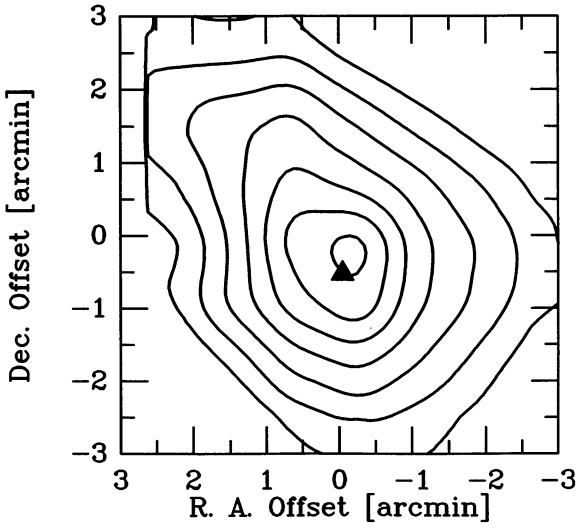

FIG. 23*a*

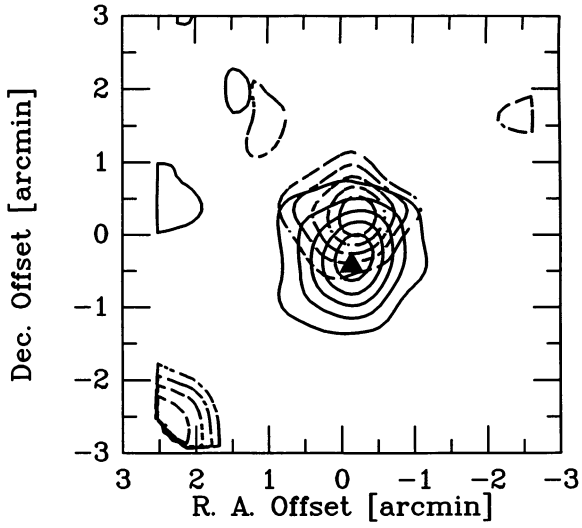

FIG. 23*b*

FIG. 23.—(*a*) Contour plot of the ^{13}CO line center integrated emission for CB 205. Contours begin at 2 K km s^{-1} and are stepped by 1 K km s^{-1}. The position of the *IRAS* PSC source is marked by a filled triangle. (*b*) Contour plot of the blue (*solid lines*) and the red (*dashed lines*) integrated line wing emission associated with CB 205/YC 1. The velocity intervals of integration were (8,13) and (18,23) km s^{-1} for the blue and the red wings, respectively. Blue contours begin at 0.8 K km s^{-1} and are stepped by 0.5 K km s^{-1}. Red contours begin at 0.7 K km s^{-1} and are stepped by 0.2 K km s^{-1}. The position of the *IRAS* PSC source is marked by a filled triangle.

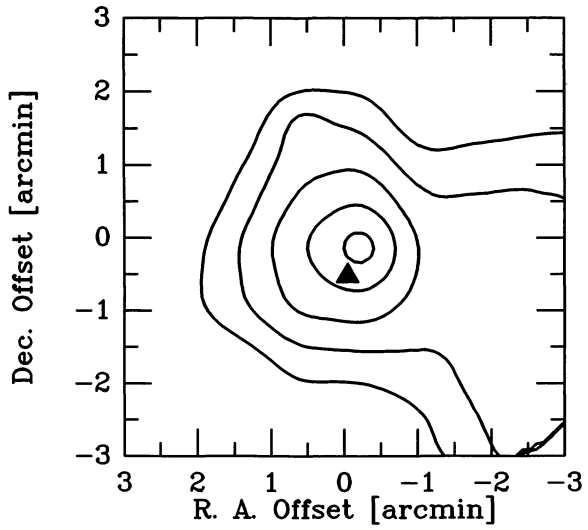

FIG. 25*a*

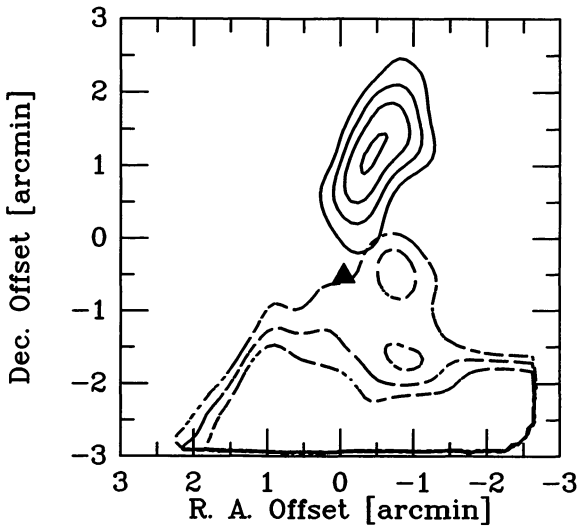

FIG. 25*b*

FIG. 25.—(*a*) Contour plot of the ^{13}CO line center integrated emission for CB 216. Contours begin at 1.5 K km s^{-1} and are stepped by 0.5 K km s^{-1}. The position of the *IRAS* PSC source is marked by a filled triangle. (*b*) Contour plot of the blue (*solid lines*) and the red (*dashed lines*) integrated line wing emission associated with CB 216/YC 1. The velocity intervals of integration were (4, 10) and (14.5, 20.0) km s^{-1} for the blue and the red wings, respectively. Blue contours begin at 0.45 K km s^{-1} and are stepped by 0.15 K km s^{-1}. Red contours begin at 0.85 K km s^{-1} and are stepped by 0.15 K km s^{-1}. The position of the *IRAS* PSC source is marked by a filled triangle.

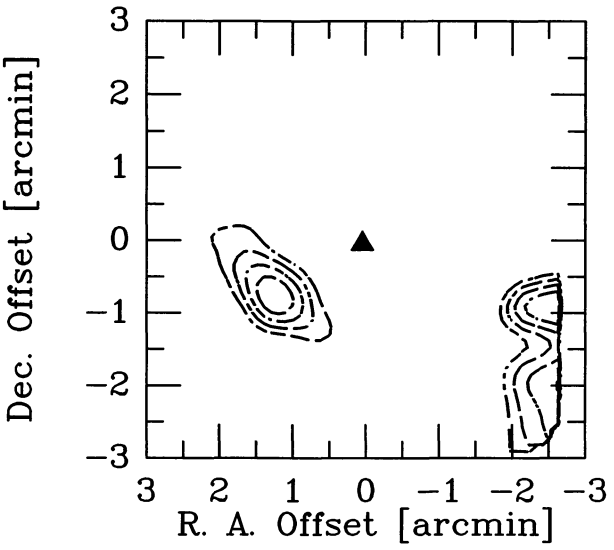

FIG. 26.—Contour plot of the red integrated line wing emission associated with CB 217/YC 1. The interval of integration was (1.5, 5.0) km s^{-1}. Contours begin at 0.45 K km s^{-1} and are stepped by 0.1 K km s^{-1}. The position of the YSO is marked by a filled triangle.

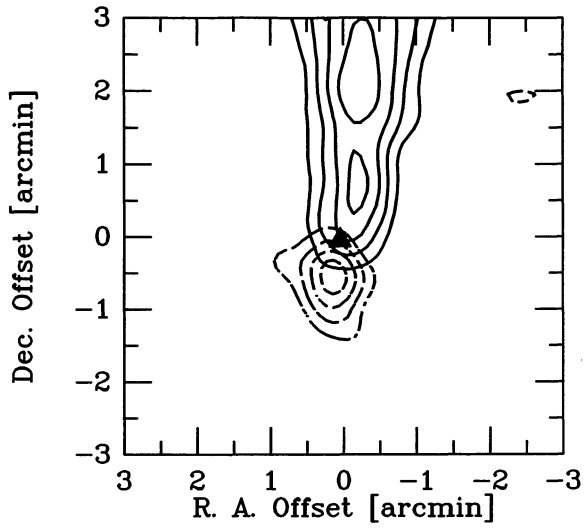

FIG. 27.—Contour plot of the blue (*solid lines*) and the red (*dashed lines*) integrated line wing emission associated with CB 230/YC 1. The velocity intervals of integration were (−1.2, 1.8) and (4, 7) km s^{-1} for the blue and the red wings, respectively. Blue contours begin at 0.25 K km s^{-1} and are stepped by 0.15 K km s^{-1}. Red contours begin at 0.5 K km s^{-1} and are stepped by 0.2 K km s^{-1}. The position of the *IRAS* PSC source is marked by a *filled triangle.*

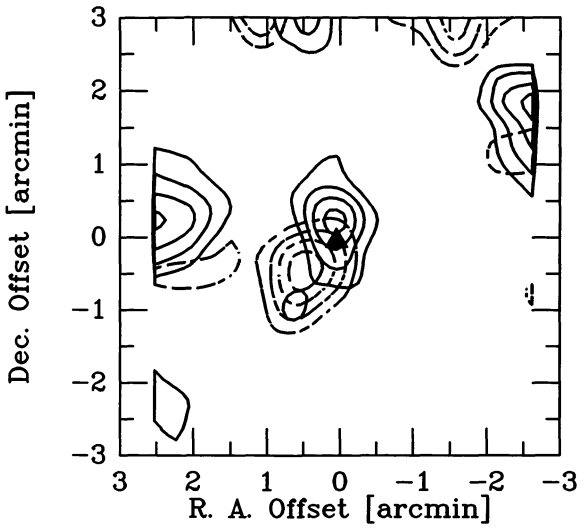

FIG. 28.—Contour plot of the blue (*solid lines*) and the red (*dashed lines*) integrated line wing emission associated with CB 232/YC 1. The velocity intervals of integration were (7,11) and (14,18) km s^{-1} for the blue and the red wings, respectively. Blue contours begin at 0.5 K km s^{-1} and are stepped by 0.2 K km s^{-1}. Red contours begin at 0.6 K km s^{-1} and are stepped by 0.2 K km s^{-1}. The position of the *IRAS* PSC source is marked by a filled triangle.

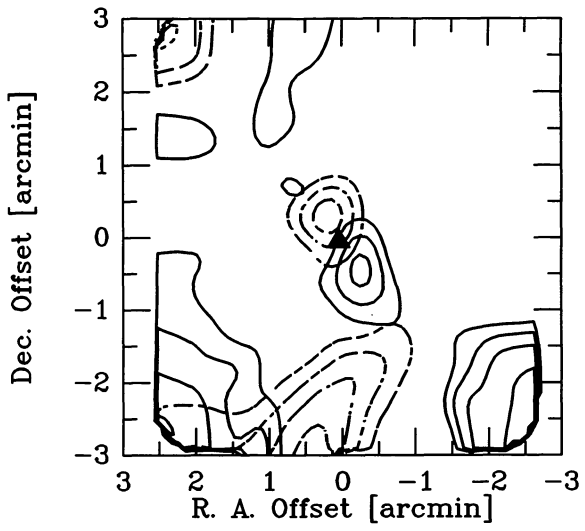

FIG. 29.—Contour plot of the blue (*solid lines*) and the red (*dashed lines*) integrated line wing emission associated with CB 244/YC 1. The velocity intervals of integration were (−2,2) and (6,10) km s^{-1} for the blue and the red wings, respectively. Blue contours begin at 0.5 K km s^{-1} and are stepped by 0.15 K km s^{-1}. Red contours begin at 0.6 K km s^{-1} and are stepped by 0.2 K km s^{-1}. The position of the *IRAS* PSC source is marked by a filled triangle.

A kinematic distance may be computed for this globule because of its large local standard of rest velocity (V_{LSR}). The direction and V_{LSR} yield a kinematic distance of ~2.1 kpc using the (R_0, θ_0) = (8.5 kpc, 220 km s^{-1}) rotation curve of Clemens (1985).

2.2. *CB 34/YC 1*

The contour map of the integrated CO line wing emission toward CB 34/YC 1 is shown in Figure 18. This outflow displays a strong blue wing (Fig. 4). The *IRAS* PSC source (*IRAS* 05440+2059), corresponding to CB 34/YC 1, is within 0.′3 of the estimated center of the outflow. Its $\alpha_{12/25}$ spectral index is −0.67 (i.e., fairly red) and no optical counterpart is seen on either of the Palomar plates.

2.3. *CB 39/YC 1*

The contour map of the integrated line wing emission of toward CB 39/YC 1 (Fig. 19) displays extended blue and red lobes which overlap significantly. Unlike CB 34/YC 1, here the red wing is more prominent, extending 8 km s^{-1} away from the line center, the largest value among the outflows found here (Fig. 5). The source of the outflow is likely to be the *IRAS* PSC source corresponding to CB 39/YC 1 (*IRAS* 05591+1630) located close to the center of the outflow. The 12/25 μm spectral index is −0.17, and there is an optical star on the red POSS, located at the *IRAS* PSC source position, which is partially surrounded by optical nebulosity, mainly NE of the source.

2.4. *CB 54/YC 1*

Figure 20 shows the CO outflow lobes toward YC 1 in the CB 54 (= LBN 1042) cloud, the most collimated outflow in this sample. The large extent of the flow and clean separation of the two projected lobes suggests that the axis of the flow may be close to being parallel to the plane of the sky. The red wing emission displays two distinct spatial peaks. The *IRAS* PSC source corresponding to CB 54/YC 1 (*IRAS* 07020−1618) is located exactly between the peak of the blue flow and the weaker peak of the red flow. If we consider the stronger NE red peak as the representative peak of the red lobe, the computed center of the outflow is shifted away from the PSC source by 0.′5 to the NE. The spectral index of the source is −0.37, and there is no POSS optical counterpart. Representative spectra are shown in Figure 6.

2.5. *CB 81/YC 1*

Because of its southern declination, the spectra obtained toward this YSO (Fig. 7) in CB 81 (= L1774) have lower signal-to-noise ratios than similar ratios for the other YSOs. The spectral lines are narrow; blue wing emission was detected ~2′ north of the *IRAS* PSC source corresponding to CB 81/YC 1 (*IRAS* 17193−2705) (Fig. 21). The spectral index of this source is −1.5 (very red), and there is no POSS optical counterpart.

2.6. *CB 188/YC 1*

The spectra obtained toward CB 188/YC 1 are presented in Figure 8. Figure 22 shows the outflow associated with CB 188/YC 1. The blue lobe overlaps the red lobe and the blue lobe is less extended. The *IRAS* PSC source corresponding to CB 188/YC 1 (*IRAS* 19179+1129) is located very close to the center of the flow. The YSO spectral index is −0.51 and it does not have an optical counterpart on the POSS.

2.7. *CB 205/YC 1*

Figure 23*a* shows the contour map of the ^{13}CO integrated emission from the globule CB 205 (= L810), revealing the location of the core of the globule. The *IRAS* PSC source corresponding to CB 205/YC 1 (*IRAS* 19433+2743) is almost coincident with the center of this ^{13}CO core.

Our CO outflow map in Figure 23*b* shows an outflow, oriented along the north-south direction, whose red and blue lobes overlap significantly.

The structure of our map agrees well with the results previously found for this outflow by Xie & Goldsmith (1990). The YSO is at the center of the ^{13}CO core and is within 0.5 of the center of the CO outflow. The infrared source has a spectral index of −0.84 and no POSS visual counterpart. There is an asymmetric optical reflection nebula, and we found a near-IR counterpart of the YSO, a symmetric near-IR nebula and a near-IR jet, which points back to the *IRAS* source (Yun et al. 1993).

2.8. *CB 214/YC 1*

Figure 24 shows the contour map of the integrated wing emission toward CB 214/YC 1. Only blueshifted wing emission was detected (Fig. 10). The extended emission at the SW corner (Fig. 24) seems to be due to a second cloud component in the wing of the line. The other edge features are artifacts of the algorithm used to create the contours. The position of the *IRAS* PSC source corresponding to CB 214/YC 1 (*IRAS* 20018+2629) is consistent with it being the origin of the outflow. It has a very negative spectral index (−1.88) and lacks an optical counterpart on the POSS plates.

2.9. *CB 216/YC 1*

The ^{13}CO integrated emission for the globule CB 216 (= L797) is shown in Figure 25*a*, revealing the location of the cloud core. The *IRAS* PSC source corresponding to CB 216/YC 1 (*IRAS* 20037+2317) is located less than 0.5 away. from the ^{13}CO peak. This source has a spectral index of −0.52 and no POSS optical counterpart.

The contour map of CO line wing emission for this YSO (Fig. 25*b*) shows well-separated blue and red lobes. The blue wing emission is concentrated to the north of the *IRAS* source, whereas the peak of the red emission is ∼1′ south of the center of the map. The extended features all along the southern edge of the map are due to contamination from a second, red component of the cloud.

2.10. *CB 217/YC 1*

CB 217 (= L863) is a very small globule. The red wing emission seen toward CB 217/YC 1 in Figure 26 is barely resolved.

There is evidence of rotation of this globule (systematic shifts in the line center velocity with position; contour maps of the mean line-core velocity reveal symmetric parallel straight lines throughout most of the cloud) and, interestingly, the axis of rotation is almost parallel to the direction connecting the peak of the red lobe to the associated YSO. This source has a positive spectral index of 0.65, and a star is visible on both the O and E Palomar plates at this position.

The component at $v = -8.5$ km s^{-1} (Fig. 12) is likely due to unrelated emission along the same line of sight.

2.11. *CB 230/YC 1*

Figure 13 reveals the presence of two CO components toward the CB 230 (= L1177) globule. In obtaining the blue integrated wing emission toward CB 230/YC 1, we have excluded the velocity interval containing the weaker cloud component $v_{LSR} \sim 3$. The resulting contour map (Fig. 27) displays a bipolar outflow with little overlap between the two lobes. Despite the high line temperatures seen in the wings, the wings do not extend very far in velocity. The position of the *IRAS* PSC source corresponding to CB 230/YC 1 (*IRAS* 21169+6804) is very close to the center of the outflow. This source has a spectral index of −0.29 and does not have a POSS optical counterpart.

2.12. *CB 232/YC 1*

Figures 14 and 28 illustrate the outflow from YC 1 in CB 232 (= B158). The spectra display well-defined wings extending ∼5 km s^{-1} away from the line center. The outflow lobes overlap and exhibit a poor degree of collimation. The *IRAS* PSC source corresponding to CB 232/YC 1 (*IRAS* 21352+4307) is located close to the center of the outflow. This source has a spectral index of −0.33 and has no POSS optical counterpart.

2.13. *CB 244/YC 1*

The outflow in this cloud was discovered by Parker, Padman, & Scott (1988) and studied interferometrically by Terebey, Myers, & Vogel (1989). When compared with the other outflow maps of this set, the contour map of the integrated line wing emission from CB 244/YC 1 (Fig. 29) shows partially overlapping lobes and a medium-collimated outflow with spectra revealing prominent red wings (Fig. 15). The peaks of the blue and red lobes are symmetrically distributed about the *IRAS* PSC source corresponding to CB 232/YC 1 (*IRAS* 23238+7401). This source has a spectral index of −0.71 and has no POSS optical counterpart.

2.14. *CB 247/YC 1*

The outflow associated with YC 1 in CB 247 (= L1263) is essentially unresolved and is detected only in three contiguous spectra at the western edge of the mapped region (two of these spectra are shown in Fig. 16). This region is centered at the PSC position of *IRAS* 23550+6430, which lies in the envelope region of the CB 247 globule, but away from its optical center. A shift of 1′ to the west would center the map at the YC position. A shift of 2′ to the west and to the north would center it at the optical center of the cloud as cataloged by CB. Therefore, we may not have observed all the area of the outflow. The *IRAS* source has a spectral index of −0.74 and no POSS optical counterpart.

3. DISCUSSION

In this section, the global properties of the set of outflows found are analyzed. The morphology of the flows is discussed,

TABLE 2

OBSERVED PROPERTIES OF DETECTED OUTFLOWS

CLOUD/YSO (1)	OUTFLOW STRUCTURE (2)	λ (3)	POSITION ANGLE (4)	OUTFLOW CENTER Δα (5)	OUTFLOW CENTER Δδ (6)	Δv (km s^{-1}) (7)
CB 3/YC 1	Bipolar	0.8	0°	−0.2	0.0	6
CB 34/YC 1	Bipolar	1.0	−15	0.2	−0.4	5
CB 39/YC 1	Red	1.2	...	...	...	5
CB 54/YC 1	Bipolar	1.4	30	0.6	0.4	7
CB 81/YC 1	Blue	0.6	...	...	...	6
CB 188/YC 1	Bipolar	1.0	75	−0.4	0.0	5
CB 205/YC 1	Blue	1.4	...	...	...	7
CB 214/YC 1	Blue	1.6	...	...	...	5
CB 216/YC 1	Bipolar	1.2	30	−1.0	0.0	6
CB 217/YC 1	Red	0.8	...	...	...	5
CB 230/YC 1	Red	0.6	...	...	...	5
CB 232/YC 1	Bipolar	1.2	−30	0.2	0.0	4
CB 244/YC 1	Bipolar	1.0	45	−0.2	−1.0	5
CB 247/YC 1	Red	1.0	...	...	...	6

and the relationships between outflow presence, spectral index, line width, and presence of a visible star are investigated. A study of the statistics of the outflow energetics concludes the analysis.

3.1. *Observed Properties and Morphology*

In Table 2 we list the YSOs with detected outflows (col. [1]) as well as estimates of the observed properties of the outflows. Column (2) indicates the outflow type. The length scale λ (col. [3]) is an estimate of the spatial extent of the outflow. This extent is the mean distance from the peak to the half-intensity contour of the integrated intensity of the high-velocity line wing of the outflow along its major axis. The velocity Δv (col. 7) lists the extent of the wings away from the line center to ~0 K. In addition, for the bipolar outflows, we indicate the position angles (on the sky, east from north) and the positions of the center of the outflows Δα and Δδ (offsets from the map centers in Table 1).

Morphologically, the outflows in our sample exhibit relatively wide angular lobes. In several cases, the red and the blue lobes overlap significantly. Using the observed sizes of the lobes, we define an apparent degree of collimation of an outflow as the ratio of the length of the observed major axis to the length of the observed minor axis. This definition coincides with the one used by several authors (e.g. Bally & Lane 1992) and makes no correction for the unknown inclination angle of the outflow axis.

With a few exceptions (e.g., CB 54/YC 1), the outflows in our set do not exhibit high degrees of apparent collimation. CB 3/YC 1, CB 39/YC 1, and CB 205/YC 1 exhibit the lowest degrees of apparent collimation. The outflows could be intrinsically more collimated than their contour maps indicate if (1) the outflows are narrower than the telescope beam, or; (2) the outflow axes are nearly along the line of sight.

However, if the outflows are intrinsically poorly collimated, and if the driving mechanism of the molecular flows is a high-velocity stellar wind, then poor collimation could be due to the lack of confinement pressure from the ambient cloud, which in several cases is about of the same size as the extent of the outflow.

In a few cases (e.g. CB 81/YC 1, CB 214/YC 1, CB 217/YC 1), the absence of one of the lobes (red or blue) may be due to the fact that the YSOs are close to cloud edges and the missing lobe extends to regions where there is little molecular material.

In all cases, the YSO have positions which make them the most likely candidates for being the source of the outflows found.

3.2. *Energetics*

A YSO in a stage of significant mass loss may alter the environment from which it formed by transferring energy and momentum to the ambient molecular cloud material. In order to investigate the possible dynamical effects of the outflows on their parent clouds and the energies required to drive the observed outflows, we have estimated the values of different dynamical parameters of the outflows: the mass M, the momentum P, the energy E, the timescale τ, the force F, the mechanical luminosity $L_{\rm mech}$, and the stellar mass-loss rate $\dot{M}_\star$. We adopt here the same value of 600 pc for the distance to all of the clouds (CB). The M, P, and E values scale with distance as $(d/600\ {\rm pc})^2$. The τ, F, $L_{\rm mech}$, and $\dot{M}_\star$ values scale with distance as $(d/600\ {\rm pc})$.

Estimates of M, P, and E are listed in Table 3. In determining these values, we have assumed that the gas is in local thermodynamical equilibrium, with a uniform excitation temperature of 10 K. We have adopted a H_2/CO abundance ratio of 10^{-4} and started by assuming optically thin line wings (to be corrected later for the average opacity in the line wings).

With these assumptions, the total column density of gas is given by $N_{H_2} = 7.3 \times 10^{19} \int T_R(v)dv\ {\rm cm}^{-2}$, where $\int T_R(v)dv$ is in K km s^{-1} (and $T_R = T_A^*/\eta_{\rm MB}$, for $\eta_{\rm MB} = 0.45$). If the line wings are optically thick, a multiplicative correction factor of $\tau/(1 - e^{-\tau})$, where τ is the mean line wing optical depth, should be applied. In principle, the line wing optical depth may be determined from the ratio of intensities in the ^{12}CO and ^{13}CO spectra. However, due to low signal-to-noise ratios in our

TABLE 3

ENERGETICS OF THE RESOLVED OUTFLOWS

YSO Outflow (1)	Mass (blue) (10^{-1} $M_\odot$) (2)	Mass (red) (10^{-1} $M_\odot$) (3)	Momentum ($M_\odot$ km s^{-1}) (4)	Energy (10^{43} ergs) (5)
CB 3/YC 1	1.8	2.2	2.8	20
CB 34/YC 1	4.0	2.0	4.2	29
CB 39/YC 1	2.9	3.1	4.8	40
CB 54/YC 1	5.5	2.0	4.4	26
CB 81/YC 1	2.7	...	1.3	7.0
CB 188/YC 1	2.7	2.4	2.0	8.0
CB 205/YC 1	3.6	2.8	5.5	46
CB 214/YC 1	4.2	...	2.2	11
CB 216/YC 1	1.6	3.3	2.8	18
CB 217/YC 1	...	1.4	0.4	1.8
CB 230/YC 1	2.4	2.2	1.7	7.0
CB 232/YC 1	2.2	2.2	2.2	11
CB 244/YC 1	2.0	2.0	2.0	10
Mean	2.9	2.4	3.0	20
Dispersion	1.1	0.6	1.5	13

^{13}CO spectra, we were unable to detect line wings in two of the three globules observed in ^{13}CO. CB 205 does display ^{13}CO line wings but due to the limited ^{13}CO signal-to-noise level, they can only be distinguished up to $\sim$4 km s^{-1} from line center, whereas the ^{12}CO line wing velocity extent is $\sim$8 km s^{-1} from line center. We have therefore adopted a typical average value of $\tau_{CO} = 3$ (Goldsmith et al. 1984) as the value of the CO optical depth averaged over the line wing velocities. The masses of the outflows were obtained by summing over each position in the maps.

The values of the momentum and energy in Table 3 represent upper limits. These were obtained using a constant outflow velocity equal to the maximum extent of the line wing velocity given in Table 2. However, no correction for the effect of the orientation of the flow relative to the line of sight was applied.

Outflow masses of the order of 0.3 $M_\odot$, outflow momenta of the order of 3 $M_\odot$ km s^{-1}, and outflow energies of the order of 10^{44} ergs were obtained. Figure 30 shows histograms of these quantities. The outflow maximum velocity has a mean of 5.8 km s^{-1} and dispersion of 1.5 km s^{-1}. The outflow total mass has a mean of 0.5 $M_\odot$ and dispersion of 0.2 $M_\odot$. The mean and dispersion of the outflow momenta are, respectively, 3.0 and 1.5 $M_\odot$ km s^{-1}. The mean and dispersion of the outflow energies are, respectively, 20 and 13 $\times$ 10^{43} ergs.

In Table 4, estimates of the dynamical parameters of the outflows are listed. The dynamical timescales τ (col. [2]) were estimated from the typical extents λ and velocities v listed in Table 2 and are of the order 10^4 yr. These values are lower limits due to the combined effects of projection angles on the sky and unknown gas accelerations. As pointed out by Cabrit & Bertout (1990), these estimates are accurate only for con-

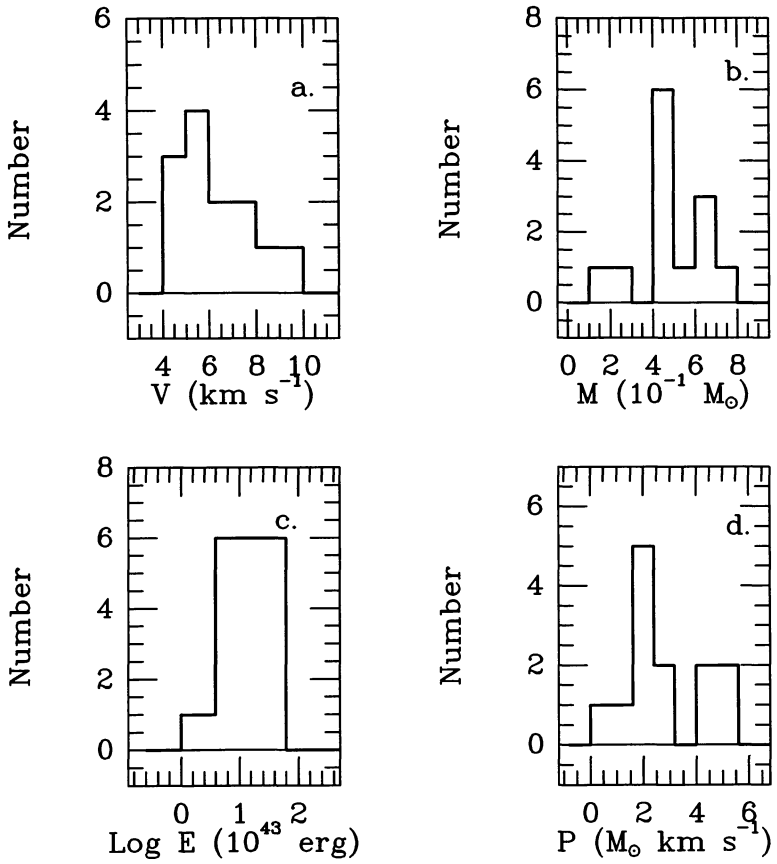

FIG. 30.—Histograms of the (*a*) outflow velocities v, (*b*) outflow masses M, (*c*) outflow energies E, and (*d*) outflow momenta P

TABLE 4

DYNAMICAL PARAMETERS OF THE RESOLVED OUTFLOWS

YSO Outflow (1)	τ (10^4 yr) (2)	F ($10^{-4}\ M_\odot$ km s^{-1} yr^{-1}) (3)	L_{mech} ($10^{-2}\ L_\odot$) (4)	$\dot{M}_\star$ ($10^{-7}\ M_\odot$ yr^{-1}) (5)
CB 3/YC 1	1.5	2.0	11	20
CB 34/YC 1	1.5	2.8	15	28
CB 39/YC 1	2.1	2.2	14	22
CB 54/YC 1	2.8	1.6	7.7	15
CB 81/YC 1	2.0	0.7	2.6	6.6
CB 188/YC 1	2.6	0.7	2.4	6.6
CB 205/YC 1	1.5	3.3	26	33
CB 214/YC 1	2.7	0.7	3.3	6.6
CB 216/YC 1	2.3	1.1	6.2	11
CB 217/YC 1	2.6	0.2	0.7	2.2
CB 230/YC 1	2.6	0.7	2.2	6.6
CB 232/YC 1	3.4	0.7	2.6	6.6
CB 244/YC 1	2.7	0.7	3.1	6.6
Mean	2.2	1.6	8.4	15
Dispersion	0.6	0.8	6.4	9

stant velocity outflows. For accelerated or decelerated outflows, timescales so calculated may underestimate the real timescales by an order of magnitude.

Assuming a steady flow during a timescale τ, the mechanical luminosity L_{mech} and force F are given by $L_{mech} = E/\tau$, and $F = P/\tau$ (cols. [3] and 4 in Table 4). Column (5) in Table 4 lists estimates of the mass loss rate $\dot{M}_\star$ of the YSOs associated with the outflows. This rate has been calculated assuming that the molecular material is swept out by a much higher velocity stellar wind of velocity $v_w \sim 100$ km s^{-1}, in an interaction where momentum is conserved [$(\dot{M}_\star = P/(\tau v_w)$].

Our estimates of outflow timescales range from 1.5 to 3.4 ×

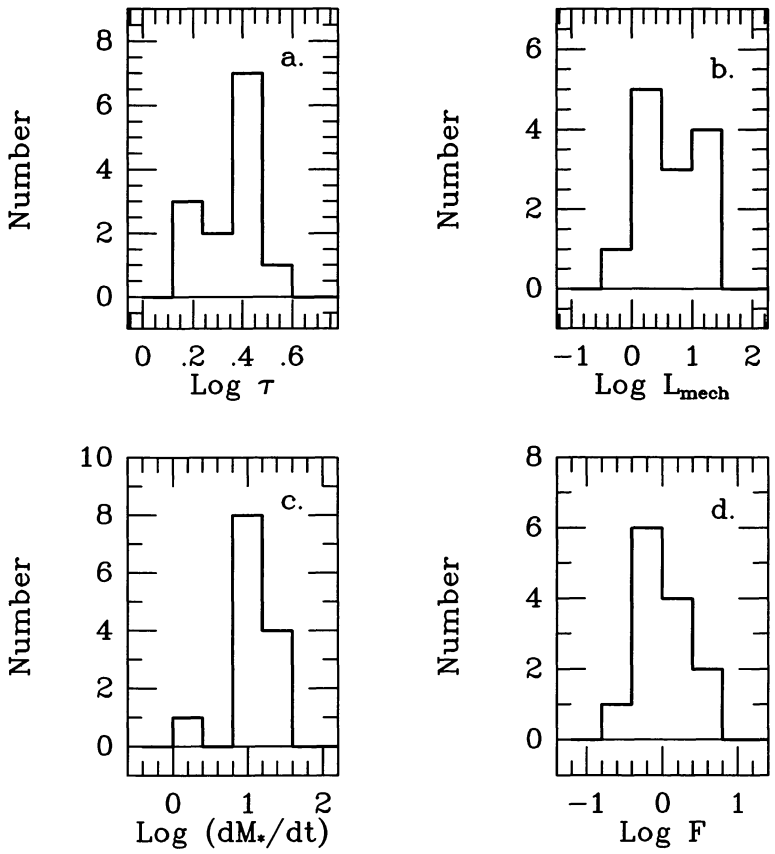

FIG. 31.—Histograms of the (*a*) outflow dynamical timescales τ; (*b*) outflow mechanical luminosities L_{mech}; (*c*) stellar mass-loss rates $\dot{M}_\star$; and (*d*) outflow forces F. The units are as in Table 4.

10^4 yr. Estimates of the mechanical luminosities and forces are $\sim 10^{-2}\ L_\odot$ and $10^{-4}\ M_\odot$ km s^{-1} yr^{-1}, respectively. Stellar mass-loss rates are of the order of $10^{-6}\ M_\odot$ yr^{-1}. Figure 31 shows the histograms of these quantities. The outflow timescale has a mean and dispersion of 2.2 and 0.6 $\times$ 10^4 yr. The outflow mechanical luminosity has a mean and dispersion of 8.4 and 6.4 $\times$ $10^{-2}\ L_\odot$. The mean and dispersion of the force are 1.6 and 0.8 $\times$ $10^{-4}\ M_\odot$ km s^{-1} yr^{-1}. The mean and dispersion of the stellar mass-loss rate are 15 and 9 $\times$ $10^{-7}\ M_\odot$ yr^{-1}.

We should point out the different sources of uncertainties that affect the values quoted in Tables 3 and 4. Standard assumptions (local thermodynamic equilibrium, uniform excitation temperature, $H_2/CO = 10^{-4}$, and $\tau/(1 - e^{-\tau}) \sim 3$) were used to estimate the different parameters. A more complete description of these techniques and related uncertainties can be found in Goldsmith et al. (1984). The two major sources of uncertainty are the unknown distances and unknown angles of inclination of the outflows. Discussion of the distances to these globules can be found in Clemens & Barvainis (1988). Finally, the accuracies of the integrated line wing intensities are noise limited. Of all these, the lack of accurate distances is by far the largest contributor to the overall uncertainties (up to an order of magnitude for the most distance sensitive quantities).

The results obtained and listed in Tables 2, 3, and 4 can be compared with similar results for molecular outflows associated with other objects. Figure 32 shows the position of several known outflows in the (M, $L_{\rm mech}$) plane, where M is the outflow mass and $L_{\rm mech}$ is the outflow mechanical luminosity. In this figure, triangles represent outflows in high-mass star formation regions. Squares, open circles, pentagons, and stars refer to outflows in dark clouds. The outflows associated with our Bok globule YSOs are represented by filled circles. If these Bok globules are close to the adopted statistical distance of 600 pc, their YSO outflows are among the weakest and least massive found to date.

The mean radius of the globules as seen on POSS prints (Clemens & Barvainis 1988) of the set of outflow globules is $\sim 2'$. Assuming a uniform sphere of density 10^4 cm^{-3} (Clemens, Yun, & Heyer 1991), this implies a gravitational self-binding energy of about 30 $\times$ 10^{43} ergs for a typical Bok globule, which is about the same order of magnitude as the average energy for the outflows. The ratios of $E_{\rm outflow}/E_{\rm gravitational}$ for our sample have a mean of $\sim$50%. This fact, together with the evidence illustrated in Paper I, that the outflows seem to typically couple well with the ambient molecular cloud, is consistent with the idea that outflows can be responsible for cloud support or dispersal, clearing the material around the forming star, perhaps setting a limit on the largest mass that can be accreted (Silk & Norman 1980; Myers et al. 1988; Fukui 1989).

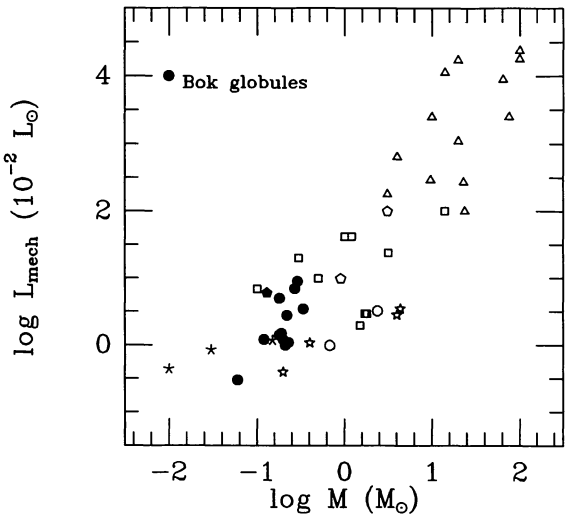

FIG. 32.—Position of several known outflows in the (M, $L_{\rm mech}$) plane. Triangles represent outflows in high-mass star formation regions (Lada 1985). *Squares* (Lada 1985), *open pentagons* (Goldsmith et al. 1984), *open stars* (Meyers et al. 1988), *centered stars* (Parker et al. 1991), and *open circles* (Knee 1992) refer to outflows from YSOs in dark clouds. The outflows associated with our sample of Bok globule YSOs are represented by filled circles. The outflow from the YSO in Bok globule B335 is represented by a filled pentagon. Outflows in Bok globules are among the weakest and least massive found.

4. SUMMARY

1. Fourteen outflows associated with YSOs in Bok globules were mapped in the J = 1–0 line of ^{12}CO using the new FCRAO QUARRY multibeam receiver. Maps of the outflows are presented as well as estimates of physical parameters of the outflows.

2. Morphologically, the outflows in our sample exhibit relatively wide angular lobes with the majority having low apparent degrees of collimation.

3. Estimates of the outflow energetics indicate that the energies involved in the outflow phenomena can be of the order of magnitude of the gravitational self-binding energies of the globules.

4. The "average" outflow in our sample has the following parameters: outflow velocity $v = (5.8 \pm 1.5)$ km s^{-1}; outflow mass $M = (0.5 \pm 0.2)\ M_\odot$; outflow timescale $\tau = (2.2 \pm 0.6) \times 10^4$ yr; outflow momentum $P = (3.0 \pm 1.5)\ M_\odot$ km s^{-1}; outflow energy $E = (20 \pm 13) \times 10^{43}$ ergs; outflow force $F = (1.6 \pm 0.8) \times 10^{-4}\ M_\odot$ km s^{-1} yr^{-1}; outflow mechanical luminosity $L_{\rm mech} = (8.4 \pm 6.4) \times 10^{-2}\ L_\odot$; and stellar mass-loss rate $\dot{M}_\star = (15 \pm 9) \times 10^{-7}\ M_\odot$ yr^{-1}, where the uncertainties presented are the sample standard deviations.

REFERENCES

Bally, J., & Lada, C. J. 1983, ApJ, 265, 824
Bally, J., & Lane, A. 1992, The Physics of Star Formation and Early Stellar Evolution, ed. C. J. Lada & N. D. Kylafis (Dordrecht: Kluwer), 471
Cabrit, S., & Bertout, C. 1990, ApJ, 348, 530
Clemens, D. P. 1985, ApJ, 295, 422
Clemens, D. P., & Barvainis, R. E. 1988, ApJS, 68, 257 (CB)
Clemens, D. P., Yun, J. L., & Heyer, M. H. 1991, ApJS, 75, 877
Erickson, N. R., Goldsmith, P. F., Novak, G., Grosslein, R. M., Viscuso, P. J., Erickson, R. B., & Predmore, C. R. 1992, IEEE MTT, Vol 40, No 1, 1
Fukui, Y. 1989, Low-Mass Star Formation and Pre-Main-Sequence Objects, ed. Bo Reipurth (Munich: ESO), 95
Goldsmith, P. F., Snell, R. J., Heyer, M. H., & Langer W. D. 1984, ApJ, 286, 599

Lada, C. J. 1985, ARA&A, 23, 267
Lada, C. J. 1987, in IAU Symp. 115, Star-Forming Regions, eds. M. Peimbert & J. Jugaku (Dordrecht: Reidel), 1
Levreault, R. M. 1988, ApJS, 67, 283
Lynds, B. T. 1962, ApJS, 7, 1
Myers, P. C., Heyer, M., Snell, R. L., & Goldsmith, P. F. 1988, ApJ, 324, 517
Parker, N. D., Padman, R., & Scott, P. F. 1991, MNRAS., 252, 442
Scappini, F., Caselli, P., & Palumbo, G. G. C. 1991, MNRAS., 249, 763
Schwartz, P. R., Gee, G., & Huang, Y. L. 1988, ApJ, 327, 350
Silk, J., & Norman, C. 1980, in IAU Symp. 87, Interstellar Molecules, (Dordrecht: Reidel), 165
Terebey, S., Myers, P. C., & Vogel, S. N. 1989, ApJ, 340, 472
Xie, T., & Goldsmith, P. F. 1990, ApJ, 359, 378
Yun, J. L., & Clemens, D. P. 1990, ApJ, 367, L76 (YC90)
———. 1992, ApJ, 385, L21 (YC92)
Yun, J. L., Clemens, D. P., McCaughrean, M., & Rieke, M. 1993, ApJ, 408, L101